Comparing electrochemical performance of transition metal silicate cathodes and chevrel phase Mo_6S_8 in the analogous rechargeable Mg-ion battery system

Xinzhi Chen[1,a], Francesca L. Bleken[2], Ole Martin Løvvik[2], Fride Vullum-Bruer[1,b]

[1]Department of Materials Science and Engineering, Norwegian University of Science and Technology, 7491 Trondheim, Norway

[2] SINTEF Materials and Chemistry, P. O. Box 124 Blindern, N-0134 Oslo, Norway

Abstract

Polyanion based silicate materials, $MgMSiO_4$ (M = Fe, Mn, Co), previously reported to be promising cathode materials for Mg-ion batteries, have been re-examined. Both the sol-gel and molten salt methods are employed to synthesize $MgMSiO_4$ composites. Mo_6S_8 is synthesized by a molten salt method combined with Cu leaching and investigated in the equivalent electrochemical system as a bench mark. Electrochemical measurements for Mo_6S_8 performed using the 2nd generation electrolyte show similar results to those reported in literature. Electrochemical performance of the silicate materials on the other hand, do not show the promising results previously reported. A thorough study of these published results are presented here, and compared to the current experimental data on the same material system. It appears that there are certain inconsistencies in the published results which cannot be explained. To further corroborate the present experimental results, atomic-scale calculations from first principles are performed, demonstrating that diffusion barriers are very high for Mg diffusion in $MgMSiO_4$. In conclusion, $MgMSiO_4$ (M = Fe, Mn, Co) olivine materials do not seem to be such good candidates for cathode materials in Mg-ion batteries as previously reported.

Keyword: Mg-ion battery; Cathode materials; Olivine; Density Functional Theory

---

[a] Current affiliation: College of Materials and Chemical Engineering, China Three Gorges University, 443002 Yichang, China

[b] vullum@nt.ntnu.no

1. Introduction

Global warming and air pollution are two of the largest environmental challenges in our time. It is a trend all over the world that we have to replace fossil fuel engines in vehicles by other more environmentally friendly techniques such as the electromotor, which can be powered by solid oxide fuel cells (SOFC), proton exchange membrane fuel cells (PEMFC), and rechargeable batteries. Among these cells rechargeable batteries are regarded as the most mature and safe solution, especially for Li-ion batteries which possess the highest practical energy density and rate capability in commercial rechargeable battery systems.[1] However, rechargeable magnesium ion batteries are currently investigated in response to several challenges of lithium ion batteries,[2] such as cost, resource availability and safety issues related to risk of thermal runaway. Lithium ion batteries have been dominating and are predicted to dominate the portable battery market in the near future due to the superior power density, while rechargeable magnesium batteries may in the short term play an important role in stationary energy storage systems and auxiliary power applications where the low cost and high reliability under a wide temperature range are more important than low weight and high power density. One potential advantage with magnesium ion batteries is that two electrons are transferred accompanying one Mg^{2+} migration, giving a theoretical specific volumetric capacity of magnesium of 3833 mAh cm^{-3}, which is close to twice that of lithium (2046 mAh cm^{-3}). [3]

Although the Mg-ion battery technology is presented as a promising complementary battery solution, there are still many challenges that need to be overcome before commercialization can be realized. First of all, suitable electrolytes which allow reversible release of Mg^{2+} ions from a magnesium metal anode are very rare. Conventional salts such as $Mg(ClO_4)_2$, $Mg(BF_4)_2$ and $Mg(CF_3SO_3)_2$ dissolved in various polar aprotic solvents result in the formation of a

passivation layer on the Mg anode and electrochemically block Mg^{2+} ion transport.[4, 5] Therefore, magnesium based electrolytes are very different compared to lithium based electrolytes and we cannot benefit from the great success of Li-ion batteries. On the other hand, even though it is well known that Grignard's reagents in ethers (RMgX, R alkyl or aryl; X Cl or Br) are capable of electrochemically depositing and dissolving magnesium,[6] it is impossible to use Grignard's reagents directly in practical Mg-ion batteries due to a too narrow electrochemical window.[3] A new electrolyte with a wide and stable electrochemical window up to 2.5 V was first developed by Aurbach et al.[7] based on Mg organo-haloaluminate salts dissolved in tetrahydrofuran (THF) or glyme based solvents, generally named as the 1st generation electrolyte. 8 years later Aurbach et al. invented the 2nd generation electrolyte with a wider electrochemical window for Mg-ion batteries,[8] which comprises the products of the reaction between PhMgCl and $AlCl_3$. Due to the presence of halides in both the 1st and 2nd generation electrolytes, these two electrolytes were also found to be corrosive [9]. Hence halide-free electrolytes were developed subsequently, like $Mg(BH_4)_2$ based electrolytes [10] and $Mg(CB_{11}H_{12})_2$/tetraglyme electrolyte system [11].

A second challenge that imposes a major barrier for commercialization of Mg-ion batteries is the development of cathode materials which should possess high capacity and high operating voltage in order to achieve sufficient energy density and power density. Screening the scientific literature reveals that several main categories can be summarized, namely, vanadium oxides, Prussian blues, molybdenum sulfide, molybdenum oxides, manganese oxides and silicates.[12] Among these materials $MgMSiO_4$ (M = Fe, Mn, Co) with an olivine structure (spacegroup *Pbnm*) [13-19] were reported to show excellent electrochemical performance with high specific capacity, high operating voltage, and good rate capability. The majority of the publications on these silicate materials are presented by the same research group, and the results are not yet

confirmed by others. One other publication comes from another research group. [20] However, their data cannot be compared to the current results as their synthesis methods lead to the production of a phase pure $MgFeSiO_4$ with a different and more open crystal structure (spacegroup *Pnma*). They also investigated different electrolytes which allowed them to perform electrochemical characterization at higher temperatures. It was therefore deemed necessary to reexamine the silicate materials as potential cathode materials in Mg-ion batteries.

It is well known that compatibility between Mg cathodes and electrolytes is very important. Thus, in this work, a widely studied chevrel phase Mo_6S_8 was employed as a standard material to establish a base line for the battery system in question. In the presented work $MgMSiO_4$ (M = Fe, Mn, Co) olivine structured silicate composites were prepared by a sol-gel method and a molten salt route. To keep consistent with literature [15-17, 19], magnesium manganese silicate is present as the nominal composition $Mg_{1.03}Mn_{0.97}SiO_4$.

2. Experimental

2.1 MgMSiO₄/C (M = Fe, Mn, Co) synthesized by a sol gel method

$MgMSiO_4$/C (M = Fe, Mn, Co) were synthesized by a wet chemical method [21], using aqueous acetate and nitrate solutions as metal precursors. The precursors used are listed in Table 1. The metal precursors were prepared by dissolving acetates and nitrate in distilled water. The concentrations of the metal cations in the aqueous precursors were determined by thermogravimetry (weight of oxide after thermal treatment). The silicon precursor solution was prepared by dissolving tetraethyl orthosilicate (TEOS) in ethanol to form a 1 mol L^{-1} solution. A polyvinyl alcohol (PVA) solution of 57 g L^{-1} was prepared by dissolving PVA in distilled water at 150 °C.

A flow chart of the synthesis route for MgMSiO$_4$/C (M = Fe, Mn, Co) is shown in Fig. 1. The standardized precursors were weighed and mixed with a molar ratio of Mg:M:Si:PVA monomer = 1:1:1:1 (Mg:Mn:Si:PVA monomer = 1.03:0.97:1:1). The mixture was vigorously stirred to form a transparent solution. A homogeneous gel was formed after stirring for 6 h at 60 °C. The as prepared gel was then covered and aged for 24 h at 25 °C before drying in the furnace for 3 h at 130 °C. The Mg-M-Si containing dry gels were calcined at 450 °C for 1 h in air. The calcined powders were then mixed with corn starch (Sigma-Aldrich, reagent grade) at a weight ratio of 7:3, using ethanol as dispersant. The as prepared powder mixtures were heat treated in a flowing Ar atmosphere at 700 °C for 10 h to obtain nanoporous MgMSiO$_4$ composites which denoted as SG-MgMSiO$_4$/C (SG-MgFeSiO$_4$/C, SG-Mg$_{1.03}$Mn$_{0.97}$SiO$_4$/C, SG-MgCoSiO$_4$/C).

	Mg precursor	Fe precursor	Mn precursor	Co precursor	Si precursor
SG-MgFeSiO$_4$/C	Mg(AC)$_2$ solution	Fe(NO$_3$)$_3$ solution	—	—	TEOS
SG-Mg$_{1.03}$Mn$_{0.97}$SiO$_4$/C	Mg(AC)$_2$ solution	—	Mn(NO$_3$)$_2$ solution	—	TEOS
SG-MgCoSiO$_4$/C	Mg(AC)$_2$ solution	—	—	Co(NO$_3$)$_2$ solution	TEOS

Table 1. Precursors to synthesize SG-MgMSiO$_4$/C (M = Fe, Mn, Co) with a sol gel method

2.2 MgMSiO$_4$/C (M = Fe, Mn, Co) and Mo$_6$S$_8$ synthesized by a molten salt method

Another series of MgMSiO$_4$/C (M = Fe, Mn, Co) were synthesized by a molten salt method, using KCl as flux to accelerate the reaction rate during the high temperature calcination. Stoichiometric amounts of the solid state precursors listed in Table 2 and KCl were mixed with a molar ratio of Mg:M:Si:KCl = 1:1:1:4 (Mg:Mn:Si:KCl = 1.03:0.97:1:4), corn starch was employed as carbon source to add into the mixtures with a 7:3 weight ratio of MgMSiO$_4$:corn starch. The as prepared powders were ball milled with ZrO$_2$ balls as medium for 6 h to ensure chemical homogeneity. The powders were further pressed into pellets which were dried at

120 °C for 12 h under vacuum to remove humidity prior to heat treating at various temperatures for 6 h with a heating rate of 2 °C min^{-1}. The sintered pellets were washed thoroughly with distilled water to remove residual KCl. Finally, fine and homogeneous MgMSiO$_4$/C (M = Fe, Mn, Co) powders were obtained after drying at 120 °C for 12 h under vacuum. The products were named as MS-MgMSiO$_4$/C (MS-MgFeSiO$_4$/C, MS-Mg$_{1.03}$Mn$_{0.97}$SiO$_4$/C, MS-MgCoSiO$_4$/C).

Copper chevrel phase Cu$_2$Mo$_6$S$_8$ was synthesized by a molten salt method using KCl as flux prior to preparing chevrel phase Mo$_6$S$_8$ by Cu leaching. Details of the methodology can be found elsewhere. [22]

	Mg precursor	Fe precursor	Mn precursor	Co precursor	Si precursor
MS-MgFeSiO$_4$/C	MgO	FeC$_2$O$_4$·2H$_2$O	—	—	SiO$_2$
MS-Mg$_{1.03}$Mn$_{0.97}$SiO$_4$/C	MgO	—	MnCO$_3$	—	SiO$_2$
MS-MgCoSiO$_4$/C	MgO	—	—	CoCO$_3$	SiO$_2$

Table 2. Precursors to synthesize MS-MgMSiO$_4$/C (M = Fe, Mn, Co) with a molten salt method

2.3 Electrolyte preparation

A so-called 2nd generation electrolyte was prepared following a standard route. This is an 'all phenyl complex' electrolyte solution (APC) [8] with a concentration of 0.4 mol L^{-1} prepared by reaction between the Lewis base PhMgCl and the Lewis acid AlCl$_3$ at a ratio of 2:1 in distilled THF.

2.4 Characterization

The specific surface area and porosity of the powders were analyzed by nitrogen adsorption measurements (Tristar 3000 Micrometrics). The qualitative X-ray diffraction was carried out with a D8 Focus X-ray diffractometer (Bruker AXS) using Cu Kα radiation (λ = 1.5406 nm) and a LynxEye PSD detector to confirm the phase purity of the powders. Fe and a Mn scripts

were applied to $MgFeSiO_4$/C and $Mg_{1.03}Mn_{0.97}SiO_4$/C samples respectively in order to reduce fluorescence. Powder morphology was examined by scanning electron microscopy (SEM) using a Hitachi S-3400 N electron microscope.

2.6 Electrochemical measurements

80 wt% of the active material, 10 wt% of super-P carbon black, and 10 wt% of polyvinylidene fluoride (PVDF) (Kynar, reagent grade) were dissolved in N-methylpyrrolidinone (NMP) and ball milled by a RETSCH mixer mill in a stainless steel container to prepare homogeneous electrode slurries. The slurries were coated onto a graphite foil (a nickel foil was used for slurry containing chevrel phase Mo_6S_8) using a tape caster and dried at 100 °C in a vacuum oven for 12 h. The active materials vary from sample to sample, but are in the range 0.42 to 4.19 mg/cm^2. Electrochemical characterization was conducted at ambient temperature with CR2016 coin cells assembled in an argon filled glove box employing magnesium alloy AZ61 as the counter electrode and Whatman® glass fiber as the separator. Assessment of electrochemical properties was done by galvanostatic charge-discharge measurements between 0.5 and 2.1 V for $MgMSiO_4$/C at 24 °C using a Maccor 4200. All reported capacities for $MgMSiO_4$/C are quoted with respect to the mass of the $MgMSiO_4$/C composites. The cyclic voltammetry (CV) measurement of the electrolyte was carried out on a Gamry electrochemical working station in the glove box under pure argon atmosphere.

2.7 Computational details

Density functional theory (DFT) calculations were performed on the *Pbnm* crystal structure of

$MgMSiO_4$ (M = Ti, V, Cr, Mn, Fe, Co, Ni, Cu, Zn). The calculations were carried out using

the Vienna *ab initio* simulation package (VASP), using plane-wave basis sets and the projector

augmented wave method to describe the core regions. [23-26] The generalized gradient

approximation (GGA) with the PBE [27] potentials was employed. Climbing image nudged

elastic band calculations were performed to identify diffusion paths and their energy barriers.

[28]

Unless otherwise stated a cut-off energy of 400 eV was used. The self-consistency criterion of

the electronic ground state was changes of the total electronic energy E_{tot} less than 10^{-5} eV for

ground state optimization, and 10^{-4} eV for NEB calculations. A **k**-point distance of 0.25 Å^{-1}

was sufficient to obtain numeric convergence of E_{tot} of 1 meV. Gaussian smearing with a width

of 0.2 eV was chosen. For ground state optimizations all calculated forces were converged

below 0.05 eV Å^{-1}. Spin was always unrestricted and the initial magnetic moment was set to 0

for Mg, Si and O and 5 for M. Pseudopotentials were chosen according to the VASP manual:

Ti_sv, V_sv, Cr_pv, Mn_pv, Fe, Co, Ni, Cu, Zn. For some elements semi-core states are treated

as valence state. They are denoted by _pv and _sv, where '3p' or '3s and 3p' states are included

as valence states, respectively. The convergence criteria were verified using the primitive unit

cell, which contains 4 Mg, 4 M, 4 Si and 16 O; this is denoted as a 1×1×1 unit cell in this study.

Various calculations on this cell were performed with M = Mn, and the unit cell shape and size

were optimized for all M with this unit cell. Except when otherwise stated, the unit cells were

held constant after the first volume optimization. 2×1×2 and 2×2×2 unit cells were compared

with results for the 1×1×1 unit cell, and screening for diffusion barriers were then performed

with the 2×1×2 unit cell.

3 Results

3.1 Phase analysis

The XRD patterns of $MgMSiO_4$/C (M = Fe, Mn, Co) powder samples obtained using a molten salt and a sol-gel method are shown in Fig. 2a and b, respectively. Samples prepared by a molten salt method show sharper peaks than those prepared by a sol-gel method, indicating a higher crystallinity and larger crystallite size, which is in good agreement with BET surface area measurement results. All samples are indexed to standard $MgMSiO_4$ (M = Fe, Mn, Co). (PDF database, 04-011-6595, $MgFeSiO_4$; PDF database, 04-015-6176, $Mg_{1.03}Mn_{0.97}SiO_4$; PDF database, 04-009-2026, $MgCoSiO_4$), no precursors or other secondary phases could be detected.

Fig. 2c shows XRD patterns of copper chevrel powder $Cu_2Mo_6S_8$ and copper leached chevrel phase Mo_6S_8, which are indexed with standard JCPDS files (PDF+ data base). However, according to Rietveld refinement, 11 % $Cu_2Mo_6S_8$ and 4 % MoS_2 are present in the final Mo_6S_8 product.

3.2 Pore morphology

The pore structure analysis based on nitrogen adsorption measurements is given in Fig. 3. The BET surface areas of samples prepared with a molten salt route are significantly lower than those samples prepared by a sol-gel method. The pore size distribution for the two series samples is also different, where mesopores and macropores both provide major contributions to the BET surface areas in the samples prepared by a sol-gel method, while the BET surface areas of samples prepared with the molten salt route are mainly due to formation of micropores. These results are consistent with data from XRD which indicate smaller crystallite sizes for the powders produced by a sol-gel method.

3.3 Electrochemical characterization

Fig. 4 shows the results of charge/discharge capacities at a rate of 0.1 C and 0.05 C for chevrel phase Mo_6S_8 and $MgMSiO_4$/C (M = Fe, Mn, Co) samples. The chevrel phase Mo_6S_8 can deliver a discharge capacity of 80 mAh g^{-1} with a distinct plateau after the first cycle, which is in good agreement with literature.[29, 30] However, $MgMSiO_4$/C (M = Fe, Mn, Co) can only deliver a discharge capacity less than 5 mAh g^{-1} after the first cycle, which is significantly lower than previous reports by Nuli et al.[13-19, 31]

3.4 Intracrystalline diffusion of Mg and M by DFT

Transition states for Mg ion diffusion were calculated for four different pathways in $MgMSiO_4$ with M = Ti, V, Cr, Mn, Fe, Co, Ni, Cu, Zn. First, diffusion of Mg in $MgMnSiO_4$ in the a- and c- directions was investigated with varying sizes of the unit cell and the plane-wave cutoff energy. Fig. 5 shows the $2\times1\times2$ unit cell (see explanation below) of the $MgFeSiO_4$ - olivine structure. The primitive unit cell contains 4 formula units, which means that the $2\times1\times2$ unit cell contains 16 Mg, 16 transition metal ions, 16 Si and 64 O, before vacancy formation.

Table 3 shows the diffusion barriers for diffusion of Mg in $MgMnSiO_4$ in the a- and c-directions calculated for the primitive unit cell and the $2\times1\times2$ and $2\times2\times2$ supercells. Note that the $2\times1\times2$ supercell is approximately cubic in size. In each system there was only one vacancy and since all Mg positions in the material without defects are equivalent, the reaction energy for diffusion was 0 in this case. (This would change if more than one vacancy were present in the unit cell as Mg positions would no longer be equivalent.)

Direction of diffusion	Size of cell (in terms of unit cell)	$\Delta E_{barrier}$ (cutoff = 400 eV) [eV]	$\Delta E_{barrier}$ (cutoff = 550 eV) [eV]

A	2×1×2	3.51	-
	2×2×2	3.56	3.55
C	1×1×1	0.85	0.86
	2×1×2	0.78	-
	2×2×2	0.78	0.74
c$^{\$}$	1×1×1	-	1.01$^{\$}$

$^{\$}$ The unit cell was relaxed at the end points, and then kept unchanged during NEB.

Table 3. Diffusion barriers for diffusion of Mg in the a- and c-directions in $MgMnSiO_4$ with various cell sizes and plane-wave cutoff energies. Start and end points are equivalent and there is therefore no reaction energy. Unit cells were kept constant when introducing vacancies.

The results show that increasing unit cell size in the b-direction did not make any significant change to any of the diffusion barriers. Also, an increase in the energy cutoff from 400 to 550 eV did not alter the results noteworthy. Further studies for $MgMSiO_4$ with M = Ti, V, Cr, Mn, Fe, Co, Ni, Cu, and Zn were therefore performed with the 2×1×2 unit cell and 400 eV cutoff. All 4 diffusion paths were calculated with 1, 3 and 5 intermediate images for M = Mn, Fe, Co and the number of initially evenly spaced out images required to obtain a correct barrier (enough images in close proximity to the barrier top) on the energy path was found to be 5 in the a- and b-directions, and 1 in the c-direction.

Barrier energies for diffusion in the a- and c- directions as well as diffusion of Mg to closest M site and of M to nearest Mg site are shown in Table 4.

Diffusing ion and direction	Mg**Ti**Si O_4	Mg**V**Si O_4	Mg**Cr** SiO_4	Mg**Mn** SiO_4	Mg**Fe** SiO_4	Mg**Co** SiO_4	Mg**Ni**Si O_4	Mg**Cu** SiO_4	Mg**Zn** SiO_4
Mg along a-axis$^{\$}$	3.52	3.88	3.34	3.51	3.81	3.80	3.97	3.59	3.78
Mg along c-axis$^{\$\$}$	0.66	0.71	0.45	0.77	0.76	0.74	0.66	0.50	0.72
Mg to M-site	0.36 (-0.92)	0.38 (-0.97)	0.03 (-0.85)	0.43 (-0.90)	0.38 (-0.92)	0.69 (-1.00)	0.35 (-0.91)	0.53 (-0.88)	0.39 (-0.95)
M to Mg-site	0.80 (0.73)	2.03 (0.92)	0.91 (0.91)	(0.88)	1.12 (0.81)	1.08 (0.80)	1.38 (0.61)	0.78 (0.78)	0.99 (0.89)

Table 4. Diffusion barrier (reaction energy when relevant) in eV for diffusion of Mg and M in MgMSiO$_4$ for M = Mn, Fe, Co. Calculations performed with 2×1×2 supercell and 400 eV cutoff. Please refer to supporting information and Fig. 6 and 7 for a visualization of these results.

For Mg diffusion along the a-direction the energy barriers are above 3 eV for all transition metals (M), with the lowest barrier for Cr (3.34 eV) and the highest barrier for Ni (3.97 eV). There is no apparent trend along the period. A visualization of this diffusion path shows that Mg diffuses in a straight path and that the surrounding SiO$_4$-tetrahedra must move to facilitate diffusion. The root mean square distance (RMSD) for all atoms except the diffusing atom was 0.116 Å for M = Fe. Files for visualization of diffusion can be found in supporting information. For diffusion in both a- and c-directions there is no energy difference between the start and end state, a result of all Mg sites being identical. The distance between Mg sites in the a- direction is 4.83 Å for M = Mn.

Mg diffusion along the c-axis presents a much lower barrier; below 0.8 eV for all transition elements. The three transition metals included in the experimental part of this study (Mn, Fe, Co) have the highest barrier (0.74 - 0.77 eV) while Cu and Cr have significantly lower barriers (0.50 and 0.45, respectively). A visualization of diffusion along the c-axis (available in supporting information) shows that in this case the Mg atom prefers a bent path, and that surrounding atoms are required to move significantly less (RMSD = 0.07 for all atoms except the diffusing Mg for M = Fe). The distance between Mg sites in the c- direction was 3.09 Å for M = Mn. It should be noted that the barrier for diffusion is lowest in the direction with closest Mg sites.

The search for Mg diffusion directly from Mg site to Mg site in the b-direction was unsuccessful, despite several different restarts, tests with different number of images, and variation of the initial configurations. Searches were performed for diffusion paths in a straight path along b and also several bent paths to the closest Mg-site, but no successful paths were identified. This was rationalized by the atomic structure between Mg sites in the b-direction, with atoms other than Mg obstructing the direct path. Also, the Mg-Mg distance is relatively large in this direction (min 5.83 Å between Mg sites with M = Mn). As an alternative path, we investigated jumps in the b direction facilitated by M vacancies (see Fig. 5). The third row in Table 4 shows the energies required to move a Mg-atom from the Mg site to a neighboring empty M-site. The number in parenthesis shows the energy difference between the start and the end states (the reaction energy). This was in all cases negative, showing that the end state is energetically more favorable. The formation energy of the M vacancy was not included, since variations between elements are prone to uncertainty due to differences in reference materials. Moving the Mg atom into a neighboring empty M site is favorable by 0.85 (Cr) - 1.00 (Co) eV per Mg atom. All energy barriers for diffusion of Mg to M-site are between 0 (Cr) and 0.7 (Co) eV. For Cr this means there is no effective barrier, while for all other transition metals the barrier is positive. This barrier is, for all M, lower than for diffusion to an empty Mg site in the c- direction. The exception is Cu, where diffusion into the empty M-site has a marginally higher barrier. Since the vacant M-site represents a favorable position for Mg, the barrier for diffusing out of this well must be the effective barrier of diffusion. This barrier is the sum of the magnitude of the reaction energy and the diffusion barrier as written in Table 4, which for Fe, Mn and Co is 1.30, 1.33 and 1.69 eV, respectively.

Mg vacancies may also be filled by atoms other than Mg. We therefore included the diffusion of the closest transition metal into a Mg vacancy. This path is analogous to that found for Mg diffusing to a metal site in the b- direction, only with switching the vacant and moving elements. Diffusion of a transition metal atom into a neighboring empty Mg-site has always a positive ΔE. The energy barrier varies more in this case compared to the three diffusion possibilities of Mg. Note that the barrier for Cr and Cu is identical to the reaction energy, showing that there is no extra diffusion barrier. V has a very high barrier of 2.03 eV, which is 1.11 eV higher than the ΔE of 0.92 eV. Examination of the structures did not show any significant differences in the diffusion paths when varying transition metal.

4. Discussion

The electrochemical performance of a Mg-ion battery is highly dependent on the intrinsic properties and utilization of active material in the electrode. The specific capacity can be expressed as:

$$C_s = \frac{C_i}{m\eta}$$ (1)

Where C_s and C_i are specific capacity and measured capacity, respectively, m and η are the mass of active material and utilization of active material, respectively. A great deal of effort was made to increase the utilization of active material. Producing nano-particulate materials and mesoporous structured materials are potential solutions to increase the active surface area and reduce the ion and electron diffusion distances, and eventually increasing the utilization of active material. Therefore, particle size and morphology are two important factors affecting the specific capacity. When particle size of chevrel phase Mo_6S_8 decreased from 0.75 to 0.57 μm, the specific capacity was increased from 71 to 84 mAh g^{-1} at a rate of 0.2 C. However, further particle size reduction did not only increase the electrochemical performances, but also decreased the specific capacity due to unwanted side reactions.[30] Feng et al. reported that

$Mg_{1.03}Mn_{0.97}SiO_4$ prepared by solid state reaction can only deliver a capacity of 43.2 mAh g^{-1} at a rate of 0.02 C (1 C = 314 mA g^{-1}), while the specific capacity of $Mg_{1.03}Mn_{0.97}SiO_4$ prepared by sol gel method can be improved up to 126 mAh g^{-1} at the rate of 0.02 C with particle size reduction. Further reduction of current density to 0.01 C can deliver a capacity as high as 244 mAh g^{-1}, [18] Zheng et al. employed three different methods (solid state reaction, molten salt and mixed solvothermal approach) to prepare $MgCoSiO_4$ with different morphologies and particle sizes. It is reported that $MgCoSiO_4$ prepared by a solvothermal approach gives the smallest particle size and a mesoporous morphology, and delivers the highest specific capacity of 167 mAh g^{-1} at a rate of 0.1 C.[13] Although particle size and morphology influence electrochemical properties, a huge difference is not expected. Our galvanostatic charge/discharge measurements show that all $MgMSiO_4$/C (M = Fe, Mn, Co) samples deliver very small capacities, almost nothing. While a normal capacity of 80 mAh g^{-1} was achieved when $MgMSiO_4$/C (M = Fe, Mn, Co) cathodes were replaced by a chevrel phase Mo_6S_8. The data for the chevrel phase materials shown here is merely to serve as a standard for our experiments and to verify that the system works as intended. No effort was therefore put into fine-tuning the synthesis to obtain more phase pure Mo_6S_8. It can be seen from the XRD data that MoS_2 (< 4%) and $Cu_2Mo_6S_8$ (~11%) are present in addition to Mo_6S_8. As expected, this is also reflected in the electrochemical performance. $Cu_2Mo_6S_8$ is known to act as a cathode for Mg-ion batteries, and since only the contribution of Mo_6S_8 was considered in our calculations this can explain why the initial discharge capacity exceeded the theoretical capacity of Mo_6S_8. It has to be noted that only the 1st generation electrolyte was used in battery systems containing $MgMSiO_4$/C (M = Fe, Mn, Co) cathode materials. The compatibility between $MgMSiO_4$ (M = Fe, Mn, Co) and the 2nd generation electrolyte (APC solution) has, to the authors' knowledge, never been reported before. The 2nd generation electrolyte has a wider electrochemical window compared to the 1st generation electrolyte (3.0 V vs. 2.5 V), and a good compatibility with

chevrel phase Mo_6S_8 has been demonstrated by several research groups [8, 29, 30], thus a good compatibility with olivine structured silicates was expected. However, based on our findings, even though the 2nd generation electrolyte has a wider electrochemical window and simpler preparation procedure, it shows poor electrochemical performances when coupled with $MgMSiO_4$/C (M = Fe, Mn, Co) cathode materials.

From Fig 4 it can be seen that all the three compositions of $MgMSiO_4$/C show an extremely small first charge capacity, while at the same time a significantly higher first cycle specific discharge capacity is observed compared to the following cycles. This might be explained by the poor diffusion of Mg^{2+} in these materials. The cell is first charged (de-magnesiated) followed by a discharge (magnesiated). Due to the slow diffusion of Mg^{2+} ions in these materials the de-intercalation will be blocked, resulting in the low charge capacity. During the first discharge on the other hand, Mg is relatively easily stripped from the Mg metal anode and deposited on the cathode surface, resulting in a much higher discharge capacity. After the first cycle a quasi-capacitor is formed, and the following charge/discharge specific capacities will be approximately equal.

It is well known that the charge can be expressed as an integration of current with respect to time.

$$q = \int_{t_0}^{t_o+\Delta t} idt \qquad (2)$$

And the scan rate can be expressed as a derivation of the potential with respect to time.

$$s = \frac{dv}{dt} \qquad (3)$$

Then the specific capacity can be described as

$$C_s = \frac{q}{m} = \frac{\int_{t_0}^{t_0+\Delta t} idt}{m} = \frac{\int_{v_0}^{v_0+\Delta v} idv}{s \cdot m} \qquad (4)$$

Where i and v are current and voltage, s and m indicate scan rate and mass of the active material, respectively. Therefore it is possible to estimate specific capacity based on the cyclic voltammogram (CV) if the scan rate is very slow (i.e. 0.1 mV/sec or slower) or if it is assumed that ion diffusion and charge exchange rate are very fast. According to this equation, comparison of estimated capacities based on the CV and galvanostatic capacities reported in the literature is shown in Table 5. $LiCrTiO_4$, $LiFePO_4$ and Mo_6S_8 were also included to verify the validity of the equation (4). The estimated specific discharge capacity of $LiFePO_4$ was 139 mAh g^{-1} at a scan rate of 0.5 mV/s, and the galvanostatic specific discharge capacity was 137 mAh g^{-1} at a current rate of 5 C. The original galvanostatic charge-discharge data of $MgFeSiO_4$ [32] indicated a specific discharge capacity of about 15 mAh g^{-1}, while a specific discharge capacity of 125 mAh g^{-1} for $MgFeSiO_4$ from galvanostatic cycling was reported by the same research group.[31] $Mn_{1.03}Mn_{0.97}SiO_4$ synthesized by a molten salt method was reported to deliver a specific capacity of 100 mAh g^{-1} at a rate of 0.2 C, however, an estimated specific capacity of 21 mAh g^{-1} was obtained according to equation (4) based on a scan rate of 50 μV/s. The estimated specific discharge capacity from cyclic voltammograms of $MgCoSiO_4$ synthesized by a molten salt method was around 1 mAh g^{-1}, while a specific discharge capacity of 123 mAh g^{-1} was reported in a galvanonstatic charge-discharge measurement.[13]

Silicates	Synthesis method	Electrolyte	Reported specific discharg capacity (mAh g^{-1})	Estimated specific discharg capacity (mAh g^{-1})	Remarks	Ref.
$MgFeSiO_4$	MS	BEC	125 (0.1C)	15 (0.1C)[1]	1C=156 mA/g	[31, 32]
	IE	MBT	330 (0.02C)[2]; 166 (0.02C)[3]	No CV data	1C=331 mA/g	[20]
$Mg_{1.03}Mn_{0.97}SiO_4$	MS (1000 °C)	BEC	100 (0.2C)	21 (50 μV/s)	1C=314.5 mA/g	[16]
	MS (800 °C)	BEC	120 (0.2C)	No CV data	1C=314.5 mA/g	[16]
	SG	BEC	80 (0.04C)	0.0004 (5 mV/s)	1C=314 mA/g	[19]
	MSG	BEC	75 (0.05C) 132 (0.02C) 239 (0.01C)	No CV data	1C=314 mA/g	[18]
	SS	BEC	62 (0.02C)	No CV data	1C=314 mA/g	[18]
	T	BEC	214 (0.2C)[4]	35 (0.1 mV/s)	1C=314 mA/g	[17]

			301 (0.2C)[5]	52 (0.1 mV/s)		
MgCoSiO$_4$	SS	BEC	70 (0.1C)	0 (0.5 mV/s)	1C=305.7 mA/g	[13]
	MS	BEC	123 (0.1C)	1 (0.5 mV/s)	1C=305.7 mA/g	[13]
	ST	BEC	167 (0.1C)	7 (0.5 mV/s)	1C=305.7 mA/g	[13]
	T	BEC	250 (0.25C); 300 (0.1C)	No CV dada	1C=305.7 mA/g	[14]
LiCrTiO$_4$	SS	LiPF$_6$_1	155 (0.1C)	170 (0.1 mV/s)	1C=157 mA/g	[33]
LiFePO4	—	LiPF$_6$_2	137 (5C)	139 (0.5 mV/s)	1C=170 mA/g	[34]
Mo$_6$S$_8$	SHS	BEC	122 (theoretical capacity)	130 (0.05 mV/s)	—	[35]

BEC---0.25 M Mg(Al$_2$BuEt)$_2$/THF; MBT---0.5 M Mg(TFSI)$_2$/CAN;
LiPF$_6$_1---1M LiPF$_6$/EC-DEC; LiPF$_6$_2---1M LiPF$_6$/EC-EMC-DMC;
MS--- a molten salt method; IE --- an ion exchange method;
SG --- a sol gel method; MSG --- a modified sol gel method;
ST--- a solvothermal method; T --- a template method;
SS --- solid state method; SHS --- self-propagating high temperature synthesis.
[1]-based on the original testing data[29] [2]-based on the three-electrode cell
[3]-based on the two-electrode cell
[4]-mesoporous Mg$_{1.03}$Mn$_{0.97}$SiO$_4$ formed from mesoporous silica SBA-15
[5]-mesoporous Mg$_{1.03}$Mn$_{0.97}$SiO$_4$ formed from mesoporous silica KIT-6

Table 5. Reported specific discharge capacities and estimated capacities from cyclic voltammogram.

For LiCrTiO$_4$, LiFePO$_4$ and Mo$_6$S$_8$ the estimated specific capacities from cyclic voltammetry are slightly higher than the reported specific capacities from galvanostatic cycling, while for MgFeSiO$_4$, Mg$_{1.03}$Mn$_{0.97}$SiO$_4$ and MgCoSiO$_4$ the estimated specific capacities are significantly lower than the reported galvanostatic specific capacities. The majority of the publications on MgMSiO$_4$ (M = Fe, Mn, Co) silicate materials is presented by Nuli's research group from 2008 to 2012, but up to now the results are not yet confirmed by others. In addition, an abnormality in peak current development with scan rate in cyclic voltammograms is reported. It is well accepted that the peak current increases with scan rate in cyclic voltammograms. However, the peak currents decrease with scan rate in the reported data by Nuli.[16]

Diffusion of Mg along the three axes of the unit cell has been studied for all three materials. The lowest barrier of Mg^{2+} diffusion was found in the c-direction (0.74 - 0.77 eV). The Mg diffusion path was slightly bent, avoiding too close contact with neighboring atoms. In contrast, the diffusion in the a-direction exhibited an extremely high energy barrier surpassing 3 eV. This involved a straight diffusion path with surrounding atoms moving in order to accommodate diffusion. The neighboring moving atoms are Si atoms being tetrahedrally coordinated to O, and as a result Si-O covalent bonds are stretched in this pathway. This results in a high energy penalty, effectively stopping diffusion. There is no apparent correlation between the barrier heights in the two directions, as seen in Fig. 6.

Diffusion in the b-direction is more complicated since the Mg atoms are not positioned along a straight line of closely spaced Mg atoms. Also diffusion in a straight line between the closest atomic positions in the b-direction is hindered by other atoms. The fact that all attempts at finding straight or bent diffusion paths in this direction were unsuccessful indicates that Mg-transport in the b-direction is very difficult. However, Fig. 7 shows that diffusion in the b-direction is permissible with empty M sites as stepping stones. The effective diffusion barrier in this direction varies from 0.88 eV (Cr) to 1.69 eV (Co). The barrier for Fe and Mn is 1.33 and 1.30 eV, respectively. Note that these barriers do not include the formation energy of the M vacancy, since there would be large uncertainty when comparing elements due to varying reference oxides. In any case, the diffusion barriers along the b-direction are far too high for any significant Mg ion diffusion to take place at room temperature.

The large difference in transition barriers in the three directions points to a major problem with these materials as effective battery electrodes. By re-examining the electronic response of the chevrel phase Mo_6S_8 cathode upon Mg intercalation, Prendergast et al. [36] found that the

metallic electronic structure of Mo_6S_8 allows highly localized electronic screening that shields the charge of Mg^{2+}, as a result, Mg^{2+} can diffuse more easily in the lattice. Their DFT calculations [36] demonstrated that the barrier of Mg^{2+} diffusion was ~ 0.5 eV in the dilute limit (one Mg in a 2×2×2 Mo_6S_8 supercell). In the present case of $MgMSiO_4$ silicates, the diffusion paths are highly anisotropic, ranging from 0.74 eV to more than 3 eV for the three directions. This is in contrast to Li silicates, where the cubic symmetry ensures isotropic barriers and the possibility of long-distance diffusion in a polycrystalline sample. The high anisotropy in Mg silicates means that the diffusion will be governed by the highest transition barriers (>3 eV), which are prohibitively large for battery applications.

Generally, these olivine structures have a mixed occupancy of 75/25 % for the Mg and M sites. Calculations performed on a 1×1×1 unit cell (4 Mg, 4 M, 16 O, 4 Si) with one Mg and M switched, gave an increase in energy of 0.12-0.14 eV, while switching all Mg and M sites gave an overall increase in energy of 0.37 eV. These are not prohibitively large numbers so a relatively large degree of mixing is expected.

Results so far have been presented with a constant volume, as we expect that a few Mg vacancies will not reduce the unit cell significantly. However, we recognize that creation of vacancies will introduce stress in the structure. Fig. 8 shows the expansion in % of volume when going from $TMSiO_4$ (all Mg removed) to $MgTMSiO_4$. The smallest expansion is observed for Ti, V and Fe.

It should be noted that when relaxing the cell with vacancies it reduces in size. As can be seen for the Mn case this increases the diffusion barrier. As our calculations are at the extreme with no cell relaxation with vacancy formation, it should be expected that the real barriers are

somewhat higher than what has been presented here. In addition it is plausible that the increase in diffusion barrier is lowest for the transitions metals with lowest unit cell change during relaxation.

5. Conclusions

Olivine structured MgMSiO$_4$/C (M = Fe, Mn, Co) materials were successfully prepared by both a sol gel and a molten salt method. Good charge/discharge properties for the chevrel phase Mo$_6$S$_8$ was found, while poor electrochemical performances for MgMSiO$_4$/C (M = Fe, Mn, Co) cathodes were demonstrated with respect to the APC electrolyte. This might indicate that the MgMSiO$_4$ (M = Fe, Mn, Co) materials are not compatible with the APC electrolyte. However, DFT calculations demonstrated that the barrier for Mg diffusion varied significantly between the three possible directions in the unit cell, from 0.74 eV to 3 eV. This indicates that the Mg diffusivity of polycrystalline silicates should be very low. By combining our experimental and modelling results with the inconsistencies found in previous publications, we conclude that Mg diffusion in MgMSiO$_4$ (M = Fe, Mn, Co) silicate cathodes is very difficult at room temperature. Our recommendation is to abandon the search for high voltage intercalation cathode materials among olivine structured Mg silicates.

References

[1] D. Aurbach, A. Schechter, M. Moshkovich, Y. Cohen, J. Electrochem. Soc. 148 (2001) A1004-A1014.

[2] P. Novák, R. Imhof, O. Haas, Electrochim. Acta, 45 (1999) 351-367.

[3] H.D. Yoo, I. Shterenberg, Y. Gofer, G. Gershinsky, N. Pour, D. Aurbach, Energy Environ. Sci. 6 (2013) 2265-2279.

[4] O.R. Brown, R. McIntyre, Electrochim. Acta 30 (1985) 627-633.

[5] Z. Lu, A. Schechter, M. Moshkovich, D. Aurbach, J. Electroanal. Chem. 466 (1999) 203-217.

[6] C. Liebenow, J. Appl. Electrochem. 27 (1997) 221-225.

[7] D. Aurbach, Z. Lu, A. Schechter, Y. Gofer, H. Gizbar, R. Turgeman, Y. Cohen, M. Moshkovich, E. Levi, Nature 407 (2000) 724-727.

[8] O. Mizrahi, N. Amir, E. Pollak, O. Chusid, V. Marks, H. Gottlieb, L. Larush, E. Zinigrad, D. Aurbach, J. Electrochem. Soc. 155 (2008) A103-A109.

[9] J. Muldoon, C.B. Bucur, A.G. Oliver, T. Sugimoto, M. Matsui, H.S. Kim, G.D. Allred, J. Zajicek, Y. Kotani, Energy Environ. Sci. 5 (2012) 5941-5950.

[10] R. Mohtadi, M. Matsui, T.S. Arthur, S.-J. Hwang, Angew. Chem. Int. Ed. 51 (2012) 9780-9783.

[11] O. Tutusaus, R. Mohtadi, T.S. Arthur, F. Mizuno, E.G. Nelson, Y.V. Sevryugina, Angew. Chem. Int. Ed. 54 (2015) 7900-7904.

[12] M.M. Huie, D.C. Bock, E.S. Takeuchi, A.C. Marschilok, K.J. Takeuchi, Coord. Chem. Rev. 287 (2015) 15-27.

[13] Y. Zheng, Y. NuLi, Q. Chen, Y. Wang, J. Yang, J. Wang, Electrochim. Acta 66 (2012) 75-81.

[14] Y. NuLi, Y. Zheng, Y. Wang, J. Yang, J. Wang, J. Mater. Chem. 21 (2011) 12437-12443.

[15] Y. NuLi, Y. Zheng, F. Wang, J. Yang, A.I. Minett, J. Wang, J. Chen, Electrochem. Commun. 13 (2011) 1143-1146.

[16] Y. NuLi, J. Yang, J. Wang, Y. Li, J. Phys. Chem. C 113 (2009) 12594-12597.

[17] Y. NuLi, J. Yang, Y. Li, J. Wang, Chem. Comm. 46 (2010) 3794-3796.

[18] Z. Feng, J. Yang, Y. NuLi, J. Wang, X. Wang, Z. Wang, Electrochem. Commun. 10 (2008) 1291-1294.

[19] Z. Feng, J. Yang, Y. NuLi, J. Wang, J. Power Sources 184 (2008) 604-609.

[20] Y. Orikasa, T. Masese, Y. Koyama, T. Mori, M. Hattori, K. Yamamoto, T. Okado, Z.-D. Huang, T. Minato, C. Tassel, J. Kim, Y. Kobayashi, T. Abe, H. Kageyama, Y. Uchimoto, Sci. Rep., 4 (2014).

[21] H. Zhou, M.-A. Einarsrud, F. Vullum-Bruer, Solid State Ionics, 225 (2012) 585-589.

[22] E. Lancry, E. Levi, Y. Gofer, M. Levi, G. Salitra, D. Aurbach, Chem. Mater. 16 (2004) 2832-2838.

[23] G. Kresse, J. Furthmüller, Comput. Mat. Sci., 6 (1996) 15.

[24] G. Kresse, J. Furthmüller, Phys. Rev. B, 54 (1996) 11169.

[25] G. Kresse, J. Hafner, Phys. Rev. B, 47 (1993) 558.

[26] G. Kresse, J. Hafner, Phys. Rev. B, 49 (1994) 14251.

[27] J.P. Perdew, K. Burke, M. Ernzerhof, Phys. Rev. Lett., 77 (1996) 3865.

[28] H. Jónsson, G. Mills, K.W. Jacobsen, Nudged Elastic Band Method for Finding Minimum Energy Paths of Transitions, in: B.J. Berne, G. Ciccotti, D.F. Coker (Eds.) Classical and Quantum Dynamics in Condensed Phase Simulations, World Scientific, 1998, pp. 385.

[29] P. Saha, P.H. Jampani, M.K. Datta, C.U. Okoli, A. Manivannan, P.N. Kumta, J. Electrochem. Soc. 161 (2014) A593-A598.

[30] A. Ryu, M.-S. Park, W. Cho, J.-S. Kim, Y.-J. Kim, Bull. Korean Chem. Soc. 34 (2013) 3033-3038.

[31] Y. Li, Y. Nuli, J. Yang, T. Yilinuer, J. Wang, Chin. Sci. Bull. 56 (2011) 386-390.

[32] Y. Li, Master thesis, (2009).

[33] V. Aravindan, W. Chuiling, S. Madhavi, J. Mater. Chem. 22 (2012) 16026-16031.

[34] H. Wang, L. Liu, R. Wang, D. Zhang, L. Zhu, S. Qiu, Y. Wei, X. Jin, Z. Zhang, J. Mater. Chem. A (2015).

[35] G. Gershinsky, O. Haik, G. Salitra, J. Grinblat, E. Levi, G. Daniel Nessim, E. Zinigrad, D. Aurbach, J. Solid State Chem. 188 (2012) 50-58.

[36] F. Thole, L.F. Wan, D. Prendergast, PCCP 17 (2015) 22548-22551.

Figure captions

Fig. 1 Flow chart of sol-gel route to synthesize $MgMSiO_4$/C (M = Fe, Mn, Co).

Fig. 2 a) XRD patterns of $MgMSiO_4$/C powder samples prepared with a molten salt route, b) XRD patterns of $MgMSiO_4$/C powder samples prepared with a sol gel method, and c) XRD patterns of (a) as prepared $Cu_2Mo_6S_8$ by a molten salt route, (b) as prepared Mo_6S_8 by Cu leaching and (c) Rietveld refinement of as prepared Mo_6S_8.

Fig. 3 Comparison of microporous surface area (S_{mic}) and external surface area ($S_{mes+mac}$) for $MgMSiO_4$/C (M = Fe, Mn, Co) powder samples made by a molten salt route and a sol-gel method, respectively.

Fig. 4 Comparison of the charge/discharge curves of $MgMSiO_4$/C (M = Fe, Mn, Co) electrodes and chevrel phase Mo_6S_8 electrode using the 2nd generation electrolyte and Mg alloy AZ61 anode.

Fig. 5 The calculated $2\times1\times2$ unit cell of $MgFeSiO_4$. The color coding for atoms is as follows: Orange = Mg, purple = Fe, blue = Si and red = O. Note the vacancy in the c- direction, shown as an example. In the b- direction two hypothetical paths are envisioned: Mg-to-Mg-site and Mg-to-Fe-site.

Fig. 6 Energy barriers in eV for diffusion of Mg to another empty Mg site in (a) a direction and (b) c-direction. Calculations performed in a $2\times1\times2$ super cell with fixed volume.

Fig. 7 Diffusion of Mg into vacant M site.[eV] The shaded (negative) bars show ΔE from start to end of diffusion. The positive bars are the barrier for diffusion of Mg from Mg site to M site. The sum of these two bars is the barrier for diffusion of Mg from M site to Mg site. Schematic representation of the three different states to the right.

Fig. 8 Unit cell expansion in % for the transition from $TMSiO_4$ to $MgTMSiO_4$, i.e. the structure with all Mg removed and the structure with no empty sites.

Figure 1

1	1	1	
Mg(AC)₂	M nitrate	TEOS	PVA

$Mg(AC)_2$ M nitrate   TEOS   PVA

Mg-M aqueous solution

TEOS ethanol solution

Mg-M-Si solution

PVA aqueous solution

Mg-M-Si-PVA gel

Gel ageing

Dry Mg-M-Si-PVA mixture

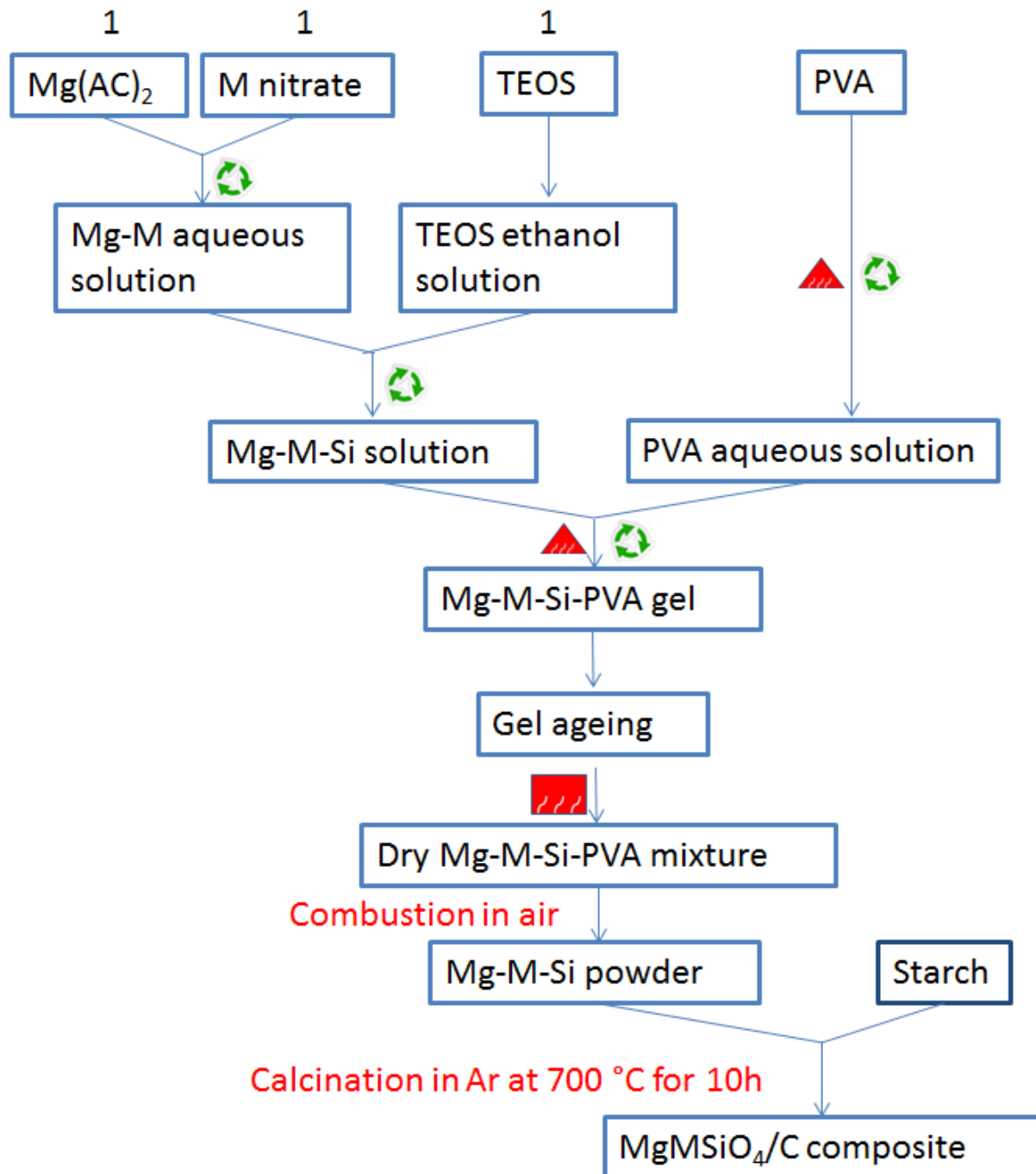Combustion in air
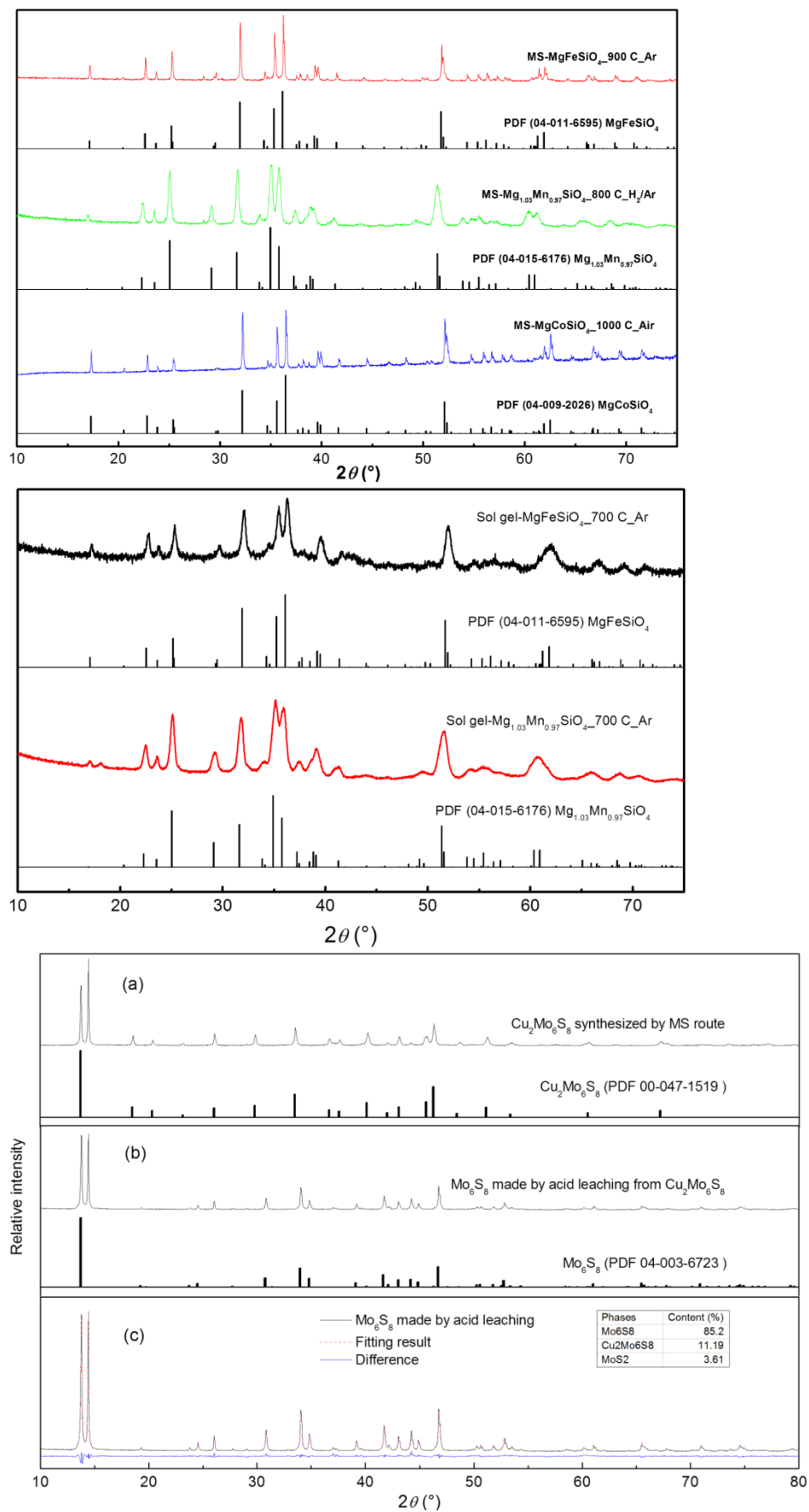
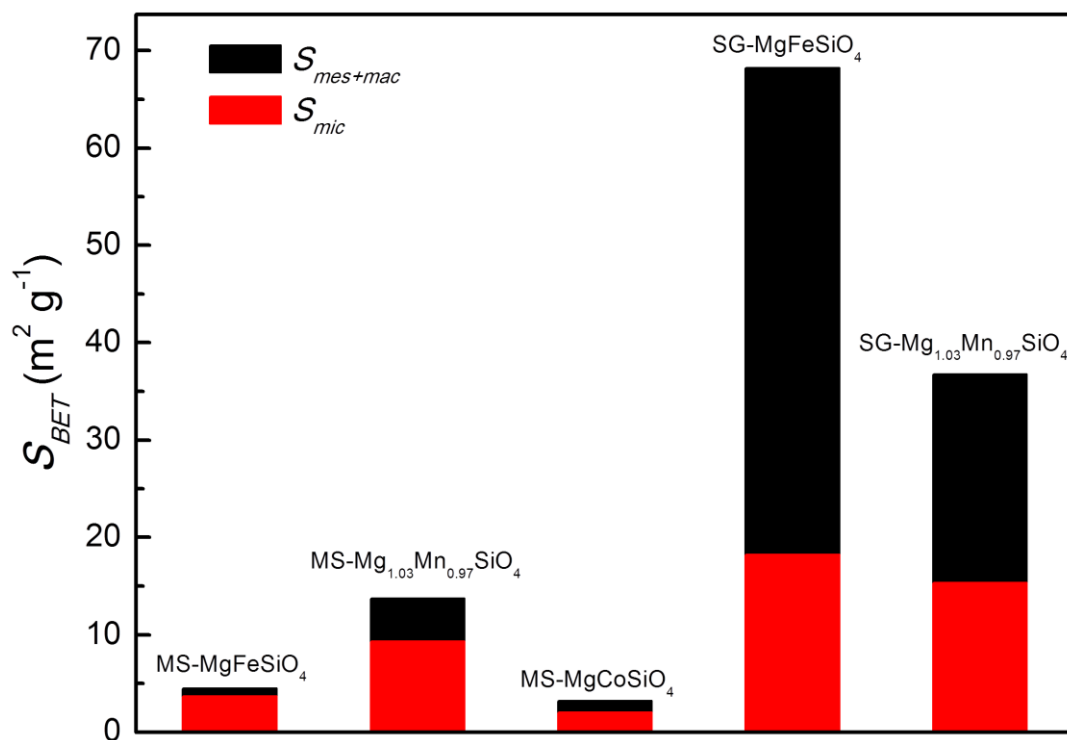Mg-M-Si powder
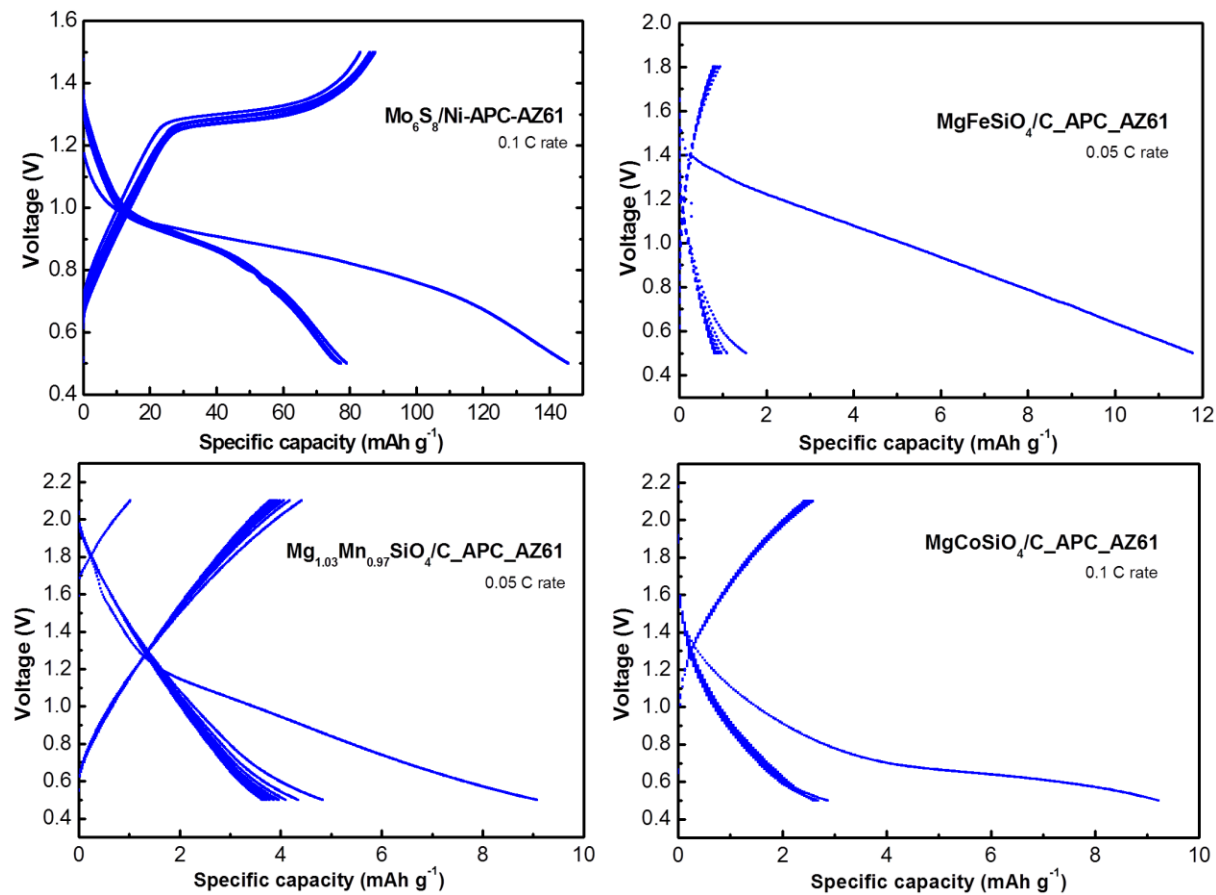
Starch

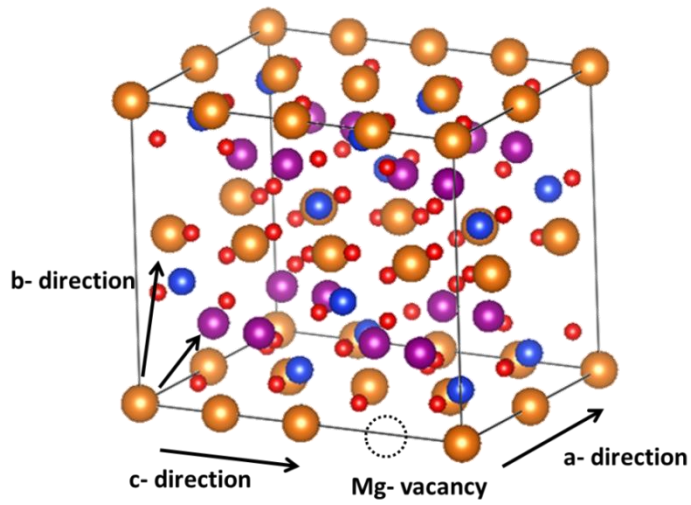Calcination in Ar at 700 °C for 10h

MgMSiO₄/C composite

Figure 2

Figure 3

Figur 4

Figure 5

Figure 6
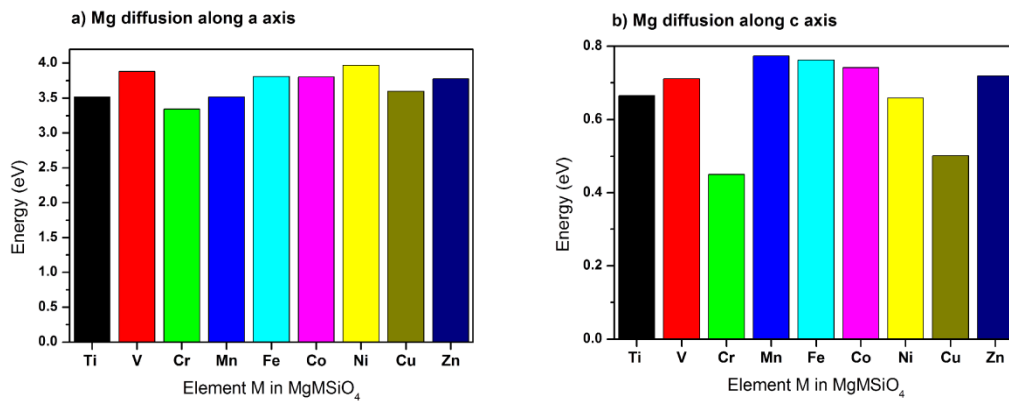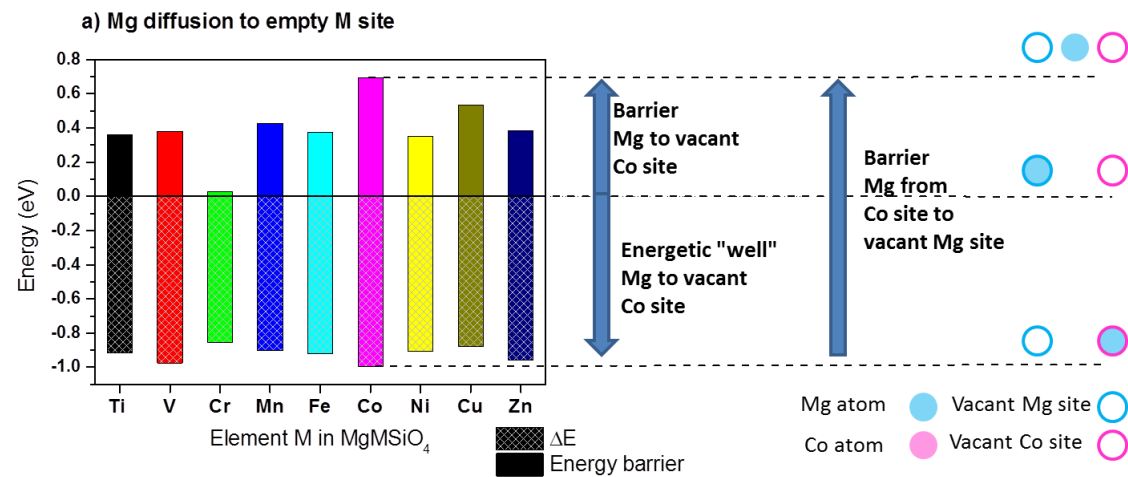

Figure 7

Figure 8

Volume expansion for 1x1x1 unit cell from $MSiO_4$ to $MgMSiO_4$

	Mg precursor	Fe precursor	Mn precursor	Co precursor	Si precursor
SG-MgFeSiO$_4$/C	Mg(AC)$_2$ solution	Fe(NO$_3$)$_3$ solution	—	—	TEOS
SG-Mg$_{1.03}$Mn$_{0.97}$SiO$_4$/C	Mg(AC)$_2$ solution	—	Mn(NO$_3$)$_2$ solution	—	TEOS
SG-MgCoSiO$_4$/C	Mg(AC)$_2$ solution	—	—	Co(NO$_3$)$_2$ solution	TEOS

Table 1. Precursors to synthesize SG-MgMSiO$_4$/C (M = Fe, Mn, Co) with a sol gel method

	Mg precursor	Fe precursor	Mn precursor	Co precursor	Si precursor
MS-MgFeSiO$_4$/C	MgO	FeC$_2$O$_4$·2H$_2$O	—	—	SiO$_2$
MS-Mg$_{1.03}$Mn$_{0.97}$SiO$_4$/C	MgO	—	MnCO$_3$	—	SiO$_2$
MS-MgCoSiO$_4$/C	MgO	—	—	CoCO$_3$	SiO$_2$

Table 2. Precursors to synthesize MS-MgMSiO$_4$/C (M = Fe, Mn, Co) with a molten salt method

Direction of diffusion	Size of cell (in terms of unit cell)	$\Delta E_{barrier}$ (cutoff = 400 eV) [eV]	$\Delta E_{barrier}$ (cutoff = 550 eV) [eV]
A	2×1×2	3.51	-
	2×2×2	3.56	3.55
C	1×1×1	0.85	0.86
	2×1×2	0.78	-
	2×2×2	0.78	0.74
c[$]	1×1×1	-	1.01[$]

[$] The unit cell was relaxed at the end points, and then kept unchanged during NEB.

Table 3. Diffusion barriers for diffusion of Mg in the a- and c-directions in MgMnSiO$_4$ with various cell sizes and plane-wave cutoff energies. Start and end points are equivalent and there is therefore no reaction energy. Unit cells were kept constant when introducing vacancies.

Diffusing ion and direction	MgTiSiO$_4$	MgVSiO$_4$	MgCrSiO$_4$	MgMnSiO$_4$	MgFeSiO$_4$	MgCoSiO$_4$	MgNiSiO$_4$	MgCuSiO$_4$	MgZnSiO$_4$
Mg along a-axis[$]	3.52	3.88	3.34	3.51	3.81	3.80	3.97	3.59	3.78
Mg along c-axis[$$]	0.66	0.71	0.45	0.77	0.76	0.74	0.66	0.50	0.72
Mg to M-site	0.36 (-0.92)	0.38 (-0.97)	0.03 (-0.85)	0.43 (-0.90)	0.38 (-0.92)	0.69 (-1.00)	0.35 (-0.91)	0.53 (-0.88)	0.39 (-0.95)
M to Mg-site	0.80 (0.73)	2.03 (0.92)	0.91 (0.91)	(0.88)	1.12 (0.81)	1.08 (0.80)	1.38 (0.61)	0.78 (0.78)	0.99 (0.89)

[$] Diffusion in slightly bent path, but minimal movement of neighboring atoms
[$$] Diffusion in straight path, but significant movement of neighboring atoms

Table 4. Diffusion barrier (reaction energy when relevant) in eV for diffusion of Mg and M in MgMSiO$_4$ for M = Mn, Fe, Co. Calculations performed with 2×1×2 supercell and 400 eV cutoff. Please refer to supporting information and Fig. 6 and 7 for a visualization of these results.

Silicates	Synthesis method	Electrolyte	Reported specific discharge capacity (mAh g^{-1})	Estimated specific discharge capacity (mAh g^{-1})	Remarks	Ref.
MgFeSiO$_4$	MS	BEC	125 (0.1C)	15 (0.1C)[1]	1C=156 mA/g	[28, 29]
	IE	MBT	330 (0.02C)[2]; 166 (0.02C)[3]	No CV data	1C=331 mA/g	[17]
Mg$_{1.03}$Mn$_{0.97}$SiO$_4$	MS (1000 °C)	BEC	100 (0.2C)	21 (50 μV/s)	1C=314.5 mA/g	[13]
	MS (800 °C)	BEC	120 (0.2C)	No CV data	1C=314.5 mA/g	[13]
	SG	BEC	80 (0.04C)	0.0004 (5 mV/s)	1C=314 mA/g	[16]
	MSG	BEC	75 (0.05C) 132 (0.02C) 239 (0.01C)	No CV data	1C=314 mA/g	[15]
	SS	BEC	62 (0.02C)	No CV data	1C=314 mA/g	[15]
	T	BEC	214 (0.2C)[4] 301 (0.2C)[5]	35 (0.1 mV/s) 52 (0.1 mV/s)	1C=314 mA/g	[14]
MgCoSiO$_4$	SS	BEC	70 (0.1C)	0 (0.5 mV/s)	1C=305.7 mA/g	[10]
	MS	BEC	123 (0.1C)	1 (0.5 mV/s)	1C=305.7 mA/g	[10]
	ST	BEC	167 (0.1C)	7 (0.5 mV/s)	1C=305.7 mA/g	[10]
	T	BEC	250 (0.25C); 300 (0.1C)	No CV dada	1C=305.7 mA/g	[11]
LiCrTiO$_4$	SS	LiPF$_6$_1	155 (0.1C)	170 (0.1 mV/s)	1C=157 mA/g	[30]
LiFePO4	—	LiPF$_6$_2	137 (5C)	139 (0.5 mV/s)	1C=170 mA/g	[31]
Mo$_6$S$_8$	SHS	BEC	122 (theoretical capacity)	130 (0.05 mV/s)	—	[32]

BEC---0.25 M Mg(Al$_2$BuEt)$_2$/THF;   MBT---0.5 M Mg(TFSI)$_2$/CAN;
LiPF$_6$_1---1M LiPF$_6$/EC-DEC;   LiPF$_6$_2---1M LiPF$_6$/EC-EMC-DMC;
MS--- a molten salt method;   IE --- an ion exchange method;
SG --- a sol gel method;   MSG --- a modified sol gel method;
ST--- a solvothermal method;   T --- a template method;
SS --- solid state method;   SHS --- self-propagating high temperature synthesis.
[1]-based on the original testing data[29]   [2]-based on the three-electrode cell
[3]-based on the two-electrode cell
[4]-mesoporous Mg$_{1.03}$Mn$_{0.97}$SiO$_4$ formed from mesoporous silica SBA-15
[5]-mesoporous Mg$_{1.03}$Mn$_{0.97}$SiO$_4$ formed from mesoporous silica KIT-6

Table 5. Reported specific discharge capacities and estimated capacities from cyclic voltammogram.